

Interferometric imaging of thermal expansion for temperature control in retinal laser therapy: supplement

DAVID VEYSSET,^{1,2,6}  TONG LING,^{1,2,3} YUEMING ZHUO,^{1,4} VIMAL PRABHU PANDIYAN,⁵  RAMKUMAR SABESAN,⁵  AND DANIEL PALANKER^{1,2,7}

¹Hansen Experimental Physics Laboratory, Stanford University, Stanford, CA 94305, USA

²Department of Ophthalmology, Stanford University, Stanford, CA 94305, USA

³Present address: School of Chemical and Biomedical Engineering, Nanyang Technological University, Singapore 637457, Singapore

⁴Department of Electrical Engineering, Stanford University, Stanford, CA 94305, USA

⁵Department of Ophthalmology, University of Washington, Seattle, WA 98109, USA

⁶dveysset@stanford.edu

⁷palanker@stanford.edu

This supplement published with Optica Publishing Group on 13 January 2022 by The Authors under the terms of the [Creative Commons Attribution 4.0 License](https://creativecommons.org/licenses/by/4.0/) in the format provided by the authors and unedited. Further distribution of this work must maintain attribution to the author(s) and the published article's title, journal citation, and DOI.

Supplement DOI: <https://doi.org/10.6084/m9.figshare.17734802>

Parent Article DOI: <https://doi.org/10.1364/BOE.448803>

Supplemental document

Interferometric imaging of thermal expansion for temperature control in retinal laser therapy

DAVID VEYSSET^{1,2,6}, TONG LING^{1,2,5}, YUEMING ZHUO^{1,3}, VIMAL PRABHU PANDIYAN⁴, RAMKUMAR SABESAN⁴, AND DANIEL PALANKER^{1,2,7}

¹Hansen Experimental Physics Laboratory, Stanford University, Stanford, CA 94305, USA

²Department of Ophthalmology, Stanford University, Stanford, CA 94305, USA

³Department of Electrical Engineering, Stanford University, Stanford, CA 94305, USA

⁴Department of Ophthalmology, University of Washington, Seattle, WA 98109, USA

⁵Present address: School of Chemical and Biomedical Engineering, Nanyang Technological University, Singapore 637457, Singapore

⁶dveysset@stanford.edu

⁷palanker@stanford.edu

© 2021 Optica Publishing Group under the terms of the [Optica Publishing Group Open Access Publishing Agreement](#)

1. Optical path lengths and lateral versus axial phase reference

The phase and optical path changes following thermal perturbation using a lateral reference point can be derived using a virtual undisturbed plane (plane V, see Fig. S1). The single-pass ΔOPL \overline{AA} is therefore the difference in optical paths between the plane A at radius r and the virtual plane (blue path in Fig. S1) and the plane A at radius r_{ref} and the virtual plane (yellow path in Fig. S1):

$$\overline{AA}(r, t) = \int_{z_V}^{z_A + u_z(r, z_A, t)} n_{air}(r, z) dz - \int_{z_V}^{z_A + u_z(r_{ref}, z_A, t)} n_{air}(r_{ref}, z) dz, \quad (\text{S1})$$

where z_A and z_V are the z -coordinates of the planes A and V, u_z is the vertical displacement (here of the plane A), n is the index of refraction of the materials (here n_{air}) along the integration paths. Assuming negligible heating of the air above the tissue phantom, n_{air} remains unchanged and equal to 1. \overline{AA} can be simplified as:

$$\overline{AA}(r, t) = z_A + u_z(r, z_A, t) - z_V - z_A - u_z(r_{ref}, z_A, t) + z_V = u_z(r, z_A, t) - u_z(r_{ref}, z_A, t). \quad (\text{S2})$$

Further assuming negligible surface displacement at radius r_{ref} gives:

$$\overline{AA}(r, t) \sim u_z(r, z_A, t). \quad (\text{S3})$$

This additional simplification step is not taken during simulations of the optical paths.

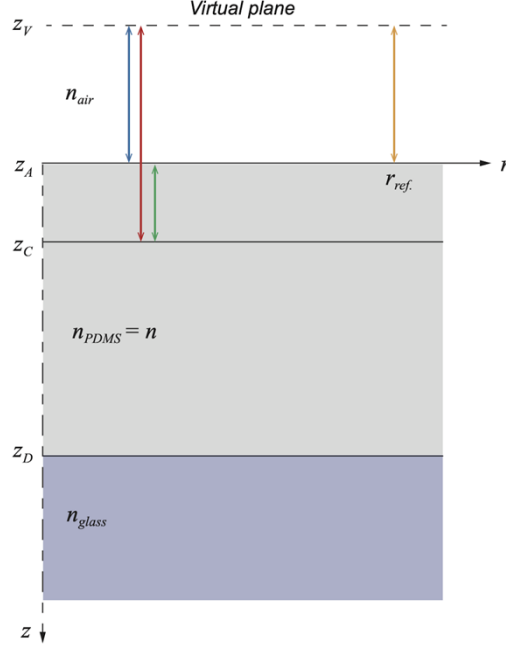


Fig. S1. OPL integration paths used to calculated \overline{AA} (blue and yellow paths), \overline{AC} (red and yellow paths), and $\overline{AC_{axial}}$ (green path).

Similarly, the \overline{AC} can be derived by subtracting the optical paths between the planes C and V at radius r (red path in Fig. S1) and the planes A and V at radius r_{ref} (yellow path in Fig. S1):

$$\overline{AC}(r, t) = \int_{z_V}^{z_C + u_z(r, z_C, t)} n(r, z) dz - \int_{z_V}^{z_A + u_z(r_{ref}, z_A, t)} n_{air}(r_{ref}, z) dz. \quad (S4)$$

The red path is split into two paths comprising the air path and the PDMS path, giving:

$$\overline{AC}(r, t) = \int_{z_V}^{z_A + u_z(r, z_A, t)} n_{air}(r, z) dz + \int_{z_A + u_z(r, z_A, t)}^{z_C + u_z(r, z_C, t)} n_{PDMS}(r, z, T(t)) dz - \int_{z_V}^{z_A + u_z(r_{ref}, z_A, t)} n_{air}(r_{ref}, z) dz. \quad (S5)$$

Along the integration path in PDMS, the index of refraction of PDMS (n_{PDMS} simplified as n) changes, because of the temperature increase θ , from $n(r, z, 23^\circ\text{C}) = n_{RT}$ (room-temperature value) to $n_{RT} + \Delta n(r, z, \theta(t))$ where $\Delta n(r, z, \theta(t)) = \alpha_{TO} \theta$ and α_{TO} is the thermo-optic coefficient. Integrating the index of refraction is equivalent to averaging its value over the integration path, then equation S5 becomes:

$$\overline{AC}(r, t) = u_z(r, z_A, t) - u_z(r_{ref}, z_A, t) + (n_{RT} + \overline{\Delta n})(z_C - z_A + u_z(r, z_C, t) - u_z(r, z_A, t)), \quad (S6)$$

where $\overline{\Delta n}$ is the average value of Δn between the planes A and C. The terms in $\overline{\Delta n} \times u_z$ are negligible, yielding:

$$\overline{AC}(r, t) = u_z(r, z_A, t) - u_z(r_{ref}, z_A, t) + n_{RT}(u_z(r, z_C, t) - u_z(r, z_A, t)) + \overline{\Delta n}(z_C - z_A) + n_{RT}(z_C - z_A). \quad (S7)$$

Again, if we consider small displacements at the radius r_{ref} , \overline{AC} can be approximated as:

$$\overline{AC}(r,t) \sim n_{RT} u_z(r, z_C, t) + (1 - n_{RT}) u_z(r, z_A, t) + \overline{\Delta n}(z_C - z_A). \quad (S8)$$

The last term $n_{RT}(z_C - z_A)$ is a constant (initial ΔOPL) and can be dropped as we are only interested in OPL changes. For \overline{AB} , C indices are replaced by B indices.

$$\overline{AB}(r,t) \sim n_{RT} u_z(r, z_B, t) + (1 - n_{RT}) u_z(r, z_A, t) + \overline{\Delta n}(z_B - z_A). \quad (S9)$$

In contrast, the axial phase difference between the planes A and C (green path in Fig. S1), which is calculated at the same radius and does not consider a lateral reference point, is:

$$\overline{AC}_{axial}(r,t) = \int_{z_A + u_z(r, z_A, t)}^{z_C + u_z(r, z_C, t)} n_{PDMS}(r, z) dz, \quad (S10)$$

$$\overline{AC}_{axial}(r,t) = n_{RT} (u_z(r, z_C, t) - u_z(r, z_A, t)) + \overline{\Delta n}(z_C - z_A) + n_{RT}(z_C - z_A) \quad (S11)$$

$$\overline{AC}_{axial}(r,t) = n_{RT} (u_z(r, z_C, t) - u_z(r, z_A, t)) + \overline{\Delta n}(z_C - z_A), \quad (S12)$$

with the constant term dropped.

2. Transfer and stiffness matrix derivation

The governing partial differential equations (PDE) of equilibrium for an elastic medium in cylindrical coordinates can be expressed as [1]:

$$\frac{\partial \sigma_r}{\partial r} + \frac{\partial \tau_{rz}}{\partial z} + \frac{\sigma_r - \sigma_\phi}{r} = 0, \quad (S13)$$

$$\frac{\partial \tau_{rz}}{\partial r} + \frac{\partial \sigma_z}{\partial z} + \frac{\tau_{rz}}{r} = 0, \quad (S14)$$

where σ_r , σ_ϕ , σ_z , are the normal stress components in the r , ϕ , and z directions and τ_{rz} is the shear stress in the r - z plane. The constitutive equations for an isotropic thermo-elastic medium are:

$$\sigma_r = \lambda \varepsilon_v + 2G \frac{\partial u_r}{\partial r} - \beta \theta, \quad (S15)$$

$$\sigma_\phi = \lambda \varepsilon_v + 2G \frac{u_r}{r} - \beta \theta, \quad (S16)$$

$$\sigma_z = \lambda \varepsilon_v + 2G \frac{\partial u_z}{\partial z} - \beta \theta, \quad (S17)$$

$$\tau_{rz} = G \left(\frac{\partial u_r}{\partial z} + \frac{\partial u_z}{\partial r} \right), \quad (S18)$$

where $G = E / (2(1 - \nu))$ is the shear modulus with E the Young's modulus and ν the Poisson's ratio; $\lambda = 2G\nu / (1 - 2\nu)$ is the Lamé's first parameter, $\varepsilon_v = \partial u_r / \partial r + u_r / r + \partial u_z / \partial z$ is the volumetric strain. The term $\beta \theta$ represents the thermal stress in which $\beta = 2G\alpha_{TE}(1 + \nu) / (1 - 2\nu)$ is the thermo-mechanical coupling parameter, and θ is the

78 temperature rise. Substituting equation S15–18 into S13–14, we obtain the following PDE
79 relating displacements and temperature:

$$80 \quad \nabla^2 u_r + \frac{1}{1-2\nu} \frac{\partial \varepsilon_v}{\partial r} - \frac{1}{r^2} u_r - \frac{\beta}{G} \frac{\partial \theta}{\partial r} = 0, \quad (\text{S19})$$

$$81 \quad \nabla^2 u_z + \frac{1}{1-2\nu} \frac{\partial \varepsilon_v}{\partial z} - \frac{\beta}{G} \frac{\partial \theta}{\partial z} = 0, \quad (\text{S20})$$

82 where $\nabla^2 = \partial^2/\partial r^2 + 1/r \partial/\partial r + \partial^2/\partial z^2$ is the Laplacian operator. We recall the heat flux
83 expression, which follows the Fourier's heat conduction law:

$$84 \quad \mathbf{q} = -\kappa \nabla \theta, \quad (\text{S21})$$

85 where $\mathbf{q} = [q_r, q_z]^T$ is the heat flux vector, κ is the coefficient of thermal conductivity, and ∇
86 is the gradient operator $\nabla = [\partial/\partial r, \partial/\partial z]^T$. The heat flow in the z direction integrated over the
87 time t is:

$$88 \quad Q = \int_0^t q_z dt. \quad (\text{S22})$$

89 The heat diffusion equation is:

$$90 \quad \frac{\partial \theta}{\partial t} = \frac{\kappa}{\rho c_p} \nabla^2 \theta = a \nabla^2 \theta, \quad (\text{S23})$$

91 where ρ is the material density, c_p is the material specific heat capacity, and $a = \kappa/(\rho c_p)$ is
92 the coefficient of thermal diffusivity.

93 Equations S19–23 can be transformed into the Hankel-Laplace (HL) domain, assuming initially
94 undisturbed media, which is required for Laplace transformation. The combined m^{th} -order
95 Hankel and Laplace transforms of a function $f(r, z, t)$ is $\tilde{f}^m(\xi, z, s)$ given by [2]:

$$96 \quad \tilde{f}^m(\xi, z, s) = \int_0^{+\infty} \int_0^{+\infty} f(r, z, t) J_m(\xi r) r e^{-st} dr dt, \quad (\text{S24})$$

97 where ξ and s are the Hankel and Laplace variables, respectively, and J_m is the m^{th} -order
98 Bessel function of the first kind. The inverse Hankel-Laplace transform is defined as:

$$99 \quad f(r, z, t) = \frac{1}{2\pi i} \int_{c-i\infty}^{c+i\infty} \int_0^{+\infty} \tilde{f}^m(\xi, z, s) J_m(\xi r) \xi e^{st} d\xi ds. \quad (\text{S25})$$

100 Taking the 1st-order Hankel and Laplace transforms of equation S19 gives:

$$101 \quad \frac{d^2 \tilde{u}_r^1}{dz^2} - \frac{2(1-\nu)}{1-2\nu} \xi^2 \tilde{u}_r^1 - \frac{1}{1-2\nu} \xi \frac{\partial \tilde{u}_z^0}{\partial z} + \frac{\beta}{G} \xi \tilde{\theta}^0 = 0, \quad (\text{S26})$$

102 and taking the 0th-order Hankel and Laplace transforms of equations S20 and S23 gives:

$$103 \quad \frac{2(1-\nu)}{1-2\nu} \frac{d^2 \tilde{u}_z^0}{dz^2} - \xi^2 \tilde{u}_z^0 + \frac{1}{1-2\nu} \xi \frac{\partial \tilde{u}_r^1}{\partial z} - \frac{\beta}{G} \frac{\partial \tilde{\theta}^0}{\partial z} = 0, \quad (\text{S27})$$

$$s\tilde{\theta}^0 - a \frac{d^2 \tilde{\theta}^0}{dz^2} + a\xi^2 \tilde{\theta}^0 = 0. \quad (\text{S28})$$

Defining a vector \mathbf{W} by:

$$\mathbf{W} = \left[\tilde{u}_r^1, \tilde{u}_z^0, \tilde{\theta}^0, \frac{d\tilde{u}_r^1}{dz}, \frac{d\tilde{u}_z^0}{dz}, \frac{d\tilde{\theta}^0}{dz} \right]^T = \left[\mathbf{\Lambda}, \frac{d\mathbf{\Lambda}}{dz} \right]^T, \quad (\text{S29})$$

where $\mathbf{\Lambda} = [\tilde{u}_r^1, \tilde{u}_z^0, \tilde{\theta}^0]^T$, equations S26–28 can be combined to obtain:

$$\frac{d\mathbf{W}(\xi, z, s)}{dz} = \mathbf{\Phi} \mathbf{W}(\xi, z, s), \quad (\text{S30})$$

with:

$$\mathbf{\Phi} = \begin{bmatrix} \mathbf{0}_{3 \times 3} & \mathbf{I}_{3 \times 3} \\ \frac{2(1-\nu)}{1-2\nu} \xi^2 & 0 & -\frac{\beta}{G} \xi & 0 & \frac{1}{1-2\nu} \xi & 0 \\ 0 & \frac{1-2\nu}{2(1-\nu)} \xi^2 & 0 & -\frac{1}{2(1-\nu)} \xi & 0 & \frac{1-2\nu}{2(1-\nu)} \frac{\beta}{G} \\ 0 & 0 & \frac{s}{a} + \xi^2 & 0 & 0 & 0 \end{bmatrix}. \quad (\text{S31})$$

$\mathbf{0}_{3 \times 3}$ is a 3×3 zero matrix and $\mathbf{I}_{3 \times 3}$ is a 3×3 identity matrix. A general solution satisfying equation S30 can be written as:

$$\mathbf{W}(\xi, z, s) = \mathbf{X}(\xi, s) e^{-\lambda z}, \quad (\text{S32})$$

where \mathbf{X} and λ are to be determined, which involves solving the eigenvalue problem:

$$\lambda \mathbf{X} = \mathbf{\Phi} \mathbf{X}. \quad (\text{S33})$$

The eigenvalues are $\lambda_1 = \xi$, $\lambda_2 = \xi$, $\lambda_3 = -\xi$, $\lambda_4 = -\xi$, $\lambda_5 = (s/a + \xi^2)^{1/2}$, and $\lambda_6 = -(s/a + \xi^2)^{1/2}$, and the corresponding solution can be written as:

$$\mathbf{W}(\xi, z, s) = (\mathbf{c}_1 + \mathbf{c}_2 z) e^{\xi z} + (\mathbf{c}_3 + \mathbf{c}_4 z) e^{-\xi z} + \mathbf{c}_5 e^{\sqrt{\frac{s}{a} + \xi^2} z} + \mathbf{c}_6 e^{-\sqrt{\frac{s}{a} + \xi^2} z}, \quad (\text{S34})$$

with:

$$\mathbf{c}_1 = \mathbf{m}_1 l_1 + \mathbf{m}_2 l_2, \quad (\text{S35})$$

$$\mathbf{c}_2 = \mathbf{m}_1 l_2, \quad (\text{S36})$$

$$\mathbf{c}_3 = \mathbf{m}_3 l_3 + \mathbf{m}_4 l_4, \quad (\text{S37})$$

$$\mathbf{c}_4 = \mathbf{m}_3 l_4, \quad (\text{S38})$$

$$\mathbf{c}_5 = \mathbf{m}_5 l_5, \quad (\text{S39})$$

$$\mathbf{c}_6 = \mathbf{m}_6 l_6, \quad (\text{S40})$$

126 where \mathbf{m}_i can be derived from the eigenvectors of Φ and l_i are arbitrary constants. For
 127 concision the vectors are not reproduced here but they are trivially derived. Considering a single
 128 finite layer, the vectors $\Lambda(\xi, z, s)$ at depth z and $\Lambda(\xi, 0, s)$ at $z = 0$ can be expressed in terms
 129 of \mathbf{L} :

$$130 \quad \begin{bmatrix} \Lambda(\xi, 0, s) \\ \Lambda(\xi, z, s) \end{bmatrix} = \begin{bmatrix} \mathbf{M}(\xi, 0, s) \\ \mathbf{M}(\xi, z, s) \end{bmatrix} \mathbf{L}, \quad (\text{S41})$$

131 with $\mathbf{L} = [l_1 \ l_2 \ l_3 \ l_4 \ l_5 \ l_6]^T$. \mathbf{M} can be derived from S34–40. The stress vector
 132 $\mathbf{V} = [\tilde{\tau}_{rz}^1, \tilde{\sigma}_z^0, \tilde{Q}^0]^T$ is related to Λ by the \mathbf{S} matrix obtained by transforming equation S17, S18,
 133 S21, and S22 into the HL domain:

$$134 \quad \tilde{\tau}_{rz}^1 = G \left(\frac{\partial \tilde{u}_r^1}{\partial z} - \xi \tilde{u}_z^0 \right), \quad (\text{S42})$$

$$135 \quad \tilde{\sigma}_z^0 = \frac{2G\nu}{1-2\nu} \xi \tilde{u}_r^1 + 2G \frac{1-\nu}{1-2\nu} \frac{\partial \tilde{u}_z^0}{\partial z} - \beta \tilde{\theta}^0, \quad (\text{S43})$$

$$136 \quad \tilde{Q}^0 = -\frac{\kappa}{s} \frac{\partial \tilde{\theta}^0}{\partial z}, \quad (\text{S44})$$

137 giving:

$$138 \quad \mathbf{V}(\xi, z, s) = \mathbf{S}(\xi, s) \mathbf{W}(\xi, z, s), \quad (\text{S45})$$

$$139 \quad \mathbf{S}(\xi, s) = \begin{bmatrix} 0 & -G\xi & 0 & G & 0 & 0 \\ \frac{2G\nu}{1-2\nu} \xi & 0 & -\beta & 0 & 2G \frac{1-\nu}{1-2\nu} & 0 \\ 0 & 0 & 0 & 0 & 0 & -\frac{\kappa}{s} \end{bmatrix}. \quad (\text{S46})$$

140 The vectors $\mathbf{V}(\xi, z, s)$ and $\mathbf{V}(\xi, 0, s)$ can also be expressed in terms of \mathbf{L} :

$$141 \quad \begin{bmatrix} -\mathbf{V}(\xi, 0, s) \\ \mathbf{V}(\xi, z, s) \end{bmatrix} = \begin{bmatrix} \mathbf{N}(\xi, 0, s) \\ \mathbf{N}(\xi, z, s) \end{bmatrix} \mathbf{L}. \quad (\text{S47})$$

142 Because Λ and \mathbf{V} can be expressed by the same constants l_i , combining S41 and S47 to
 143 eliminate \mathbf{L} yields the relationship between the state vectors through the stiffness matrix \mathbf{K} :

$$144 \quad \begin{bmatrix} -\mathbf{V}(\xi, 0, s) \\ \mathbf{V}(\xi, z, s) \end{bmatrix} = \mathbf{K} \begin{bmatrix} \Lambda(\xi, 0, s) \\ \Lambda(\xi, z, s) \end{bmatrix}. \quad (\text{S48})$$

145 The elements in \mathbf{K} , which depends on the materials properties of the natural layer and the
 146 depth z in the layer, also given in [3]^a, are:

^a A typo exists in the element \mathbf{K}_{23} in reference [3] and is corrected here

$$\mathbf{K}_{11} = \mathbf{K}_{44} = \frac{2G\xi b_2 (4z\xi e_1^2 b_1 - b_3 d_1 d_3)}{g}, \quad (\text{S49})$$

$$\mathbf{K}_{12} = \mathbf{K}_{21} = -\mathbf{K}_{45} = -\mathbf{K}_{54} = \frac{2G\xi (4z^2 \xi^2 e_1^2 b_1^2 - Gb_3 d_1^2)}{g}, \quad (\text{S50})$$

$$\mathbf{K}_{13} = \mathbf{K}_{46} = -\frac{2G\beta a \xi (4z\xi e_1 b_1 (pe_2 d_1 - \xi e_1 d_2) + b_3 d_1 (\xi d_2 d_3 - pd_1 d_4))}{sgd_2}, \quad (\text{S51})$$

$$\mathbf{K}_{14} = \mathbf{K}_{41} = \frac{4G\xi e_1 b_2 (b_3 d_1 - z\xi b_1 d_3)}{g}, \quad (\text{S52})$$

$$\mathbf{K}_{15} = \mathbf{K}_{51} = -\mathbf{K}_{24} = -\mathbf{K}_{42} = \frac{-4Gz\xi^2 e_1 b_1 b_2 d_1}{g}, \quad (\text{S53})$$

$$\mathbf{K}_{16} = \mathbf{K}_{43} = \frac{-4G\beta a \xi (z\xi e_1 b_1 (\xi d_2 d_3 - pd_1 d_4) + b_3 d_1 (pe_2 d_1 - \xi e_1 d_2))}{sgd_2}, \quad (\text{S54})$$

$$\mathbf{K}_{22} = \mathbf{K}_{55} = \frac{-2G\xi b_2 (4z\xi e_1^2 b_1 + b_3 d_1 d_3)}{g}, \quad (\text{S55})$$

$$\mathbf{K}_{23} = -\mathbf{K}_{56} = \frac{2G\beta a \xi (4z\xi pe_1 b_1 f + 4pe_1 e_2 b_3 d_1 + b_3 d_1 (\xi d_1 d_2 - pd_3 d_4))}{sgd_2}, \quad (\text{S56})$$

$$\mathbf{K}_{25} = \mathbf{K}_{52} = \frac{4G\xi e_1 b_2 (b_3 d_1 + z\xi b_1 d_3)}{g}, \quad (\text{S57})$$

$$\mathbf{K}_{26} = -\mathbf{K}_{53} = \frac{4G\beta a \xi (4z\xi pe_1^2 e_2 b_1 + z\xi e_1 b_1 (\xi d_1 d_2 - pd_3 d_4) + pb_3 d_1 f)}{sgd_2}, \quad (\text{S58})$$

$$\mathbf{K}_{33} = \mathbf{K}_{66} = \frac{-\kappa pd_4}{sd_2}, \quad (\text{S59})$$

$$\mathbf{K}_{36} = \mathbf{K}_{63} = \frac{2\kappa pe_2}{sd_2}, \quad (\text{S60})$$

$$\mathbf{K}_{13} = \mathbf{K}_{32} = \mathbf{K}_{34} = \mathbf{K}_{35} = \mathbf{K}_{61} = \mathbf{K}_{62} = \mathbf{K}_{64} = \mathbf{K}_{65} = 0, \quad (\text{S61})$$

where $p = (s/a + \xi^2)^{1/2}$, $b_1 = \lambda + G$, $b_2 = \lambda + 2G$, $b_3 = \lambda + 3G$, $e_1 = e^{-z\xi}$, $e_2 = e^{-zp}$,
 $d_1 = 1 - e_1^2$, $d_2 = 1 - e_2^2$, $d_3 = 1 + e_1^2$, $d_4 = 1 + e_2^2$, $f = e_2 d_3 - e_1 d_4$, $g = 4z^2 \xi^2 e_1^2 b_1^2 - b_3^2 d_1^2$.

More generally, for a multi-layered medium, the relationship between planes at depth h_i and h_{i+1} within a finite layer made of a single material is:

$$\begin{bmatrix} -\mathbf{V}(\xi, h_i, s) \\ \mathbf{V}(\xi, h_{i+1}, s) \end{bmatrix} = \mathbf{K}^{(k)} \begin{bmatrix} \mathbf{\Lambda}(\xi, h_i, s) \\ \mathbf{\Lambda}(\xi, h_{i+1}, s) \end{bmatrix}, \quad (\text{S62})$$

165 where $\mathbf{K}^{(k)}$ is the stiffness matrix of the k -th layer. Therefore, for our tissue phantom, depicted
 166 in Fig. S2, the relationship between the state vectors at depth $z_A = 0$, z_C , z_D , z_E can be
 167 expressed as follows:

$$168 \quad \begin{bmatrix} -\mathbf{V}(\xi, 0^+, s) \\ \mathbf{V}(\xi, z_c^-, s) \end{bmatrix} = \mathbf{K}^{(1,2)} \begin{bmatrix} \Lambda(\xi, 0^+, s) \\ \Lambda(\xi, z_c^-, s) \end{bmatrix}, \quad (\text{S63})$$

$$169 \quad \begin{bmatrix} -\mathbf{V}(\xi, z_c^+, s) \\ \mathbf{V}(\xi, z_D^-, s) \end{bmatrix} = \mathbf{K}^{(3,4)} \begin{bmatrix} \Lambda(\xi, z_c^+, s) \\ \Lambda(\xi, z_D^-, s) \end{bmatrix}, \quad (\text{S64})$$

$$170 \quad \begin{bmatrix} -\mathbf{V}(\xi, z_D^+, s) \\ \mathbf{V}(\xi, z_E^-, s) \end{bmatrix} = \mathbf{K}^{(5)} \begin{bmatrix} \Lambda(\xi, z_D^+, s) \\ \Lambda(\xi, z_E^-, s) \end{bmatrix}, \quad (\text{S65})$$

171 where $\mathbf{K}^{(1,2)}$, $\mathbf{K}^{(3,4)}$, $\mathbf{K}^{(5)}$ are the stiffness matrices corresponding to the combined layers 1
 172 and 2, and 3 and 4, and the layer 5. Layers 1 and 2, and 3 and 4 can be combined as we assume
 173 the same materials properties for those PMDS layers. For the top and bottom half-spaces, the
 174 relationship between the state vectors can be simplified to:

$$175 \quad \mathbf{V}(\xi, 0^-, s) = \mathbf{K}^{(-\infty)} \Lambda(\xi, 0^-, s), \quad (\text{S66})$$

176 and:

$$177 \quad -\mathbf{V}(\xi, z_E^+, s) = \mathbf{K}^{(+\infty)} \Lambda(\xi, z_E^+, s), \quad (\text{S67})$$

178 which consider no stress, displacement, heat transfer, or temperature rise at infinity:

$$179 \quad \mathbf{V}(\xi, -\infty, s) = \mathbf{V}(\xi, +\infty, s) = \Lambda(\xi, -\infty, s) = \Lambda(\xi, +\infty, s) = 0. \quad (\text{S68})$$

180 $\mathbf{K}^{(+\infty)}$ and $\mathbf{K}^{(-\infty)}$ are 3×3 submatrices of \mathbf{K} with:

$$181 \quad \mathbf{K}^{(+\infty)} = \lim_{z \rightarrow +\infty} \begin{bmatrix} \mathbf{K}_{11} & \mathbf{K}_{12} & \mathbf{K}_{13} \\ \mathbf{K}_{21} & \mathbf{K}_{22} & \mathbf{K}_{23} \\ \mathbf{K}_{31} & \mathbf{K}_{32} & \mathbf{K}_{33} \end{bmatrix} = \begin{bmatrix} \mathbf{K}_{11}^{(+\infty)} & \mathbf{K}_{12}^{(+\infty)} & \mathbf{K}_{13}^{(+\infty)} \\ \mathbf{K}_{21}^{(+\infty)} & \mathbf{K}_{22}^{(+\infty)} & \mathbf{K}_{23}^{(+\infty)} \\ \mathbf{K}_{31}^{(+\infty)} & \mathbf{K}_{32}^{(+\infty)} & \mathbf{K}_{33}^{(+\infty)} \end{bmatrix}, \quad (\text{S69})$$

$$182 \quad \mathbf{K}_{11}^{(+\infty)} = \mathbf{K}_{22}^{(+\infty)} = 2G\xi b_2 / b_3, \quad (\text{S70})$$

$$183 \quad \mathbf{K}_{12}^{(+\infty)} = \mathbf{K}_{21}^{(+\infty)} = -2G^2\xi / b_3, \quad (\text{S71})$$

$$184 \quad \mathbf{K}_{13}^{(+\infty)} = \mathbf{K}_{23}^{(+\infty)} = 2G\beta a\xi(\xi - p) / sb_3, \quad (\text{S72})$$

$$185 \quad \mathbf{K}_{31}^{(+\infty)} = \mathbf{K}_{32}^{(+\infty)} = 0, \quad (\text{S73})$$

$$186 \quad \mathbf{K}_{33}^{(+\infty)} = -\kappa p / s, \quad (\text{S74})$$

187 and:

$$\mathbf{K}^{(-\infty)} = \lim_{z \rightarrow +\infty} \begin{bmatrix} \mathbf{K}_{44} & \mathbf{K}_{45} & \mathbf{K}_{46} \\ \mathbf{K}_{54} & \mathbf{K}_{55} & \mathbf{K}_{56} \\ \mathbf{K}_{64} & \mathbf{K}_{65} & \mathbf{K}_{66} \end{bmatrix} = \begin{bmatrix} \mathbf{K}_{11}^{(+\infty)} & -\mathbf{K}_{12}^{(+\infty)} & \mathbf{K}_{13}^{(+\infty)} \\ -\mathbf{K}_{21}^{(+\infty)} & \mathbf{K}_{22}^{(+\infty)} & -\mathbf{K}_{23}^{(+\infty)} \\ \mathbf{K}_{31}^{(+\infty)} & -\mathbf{K}_{32}^{(+\infty)} & \mathbf{K}_{33}^{(+\infty)} \end{bmatrix}. \quad (\text{S75})$$

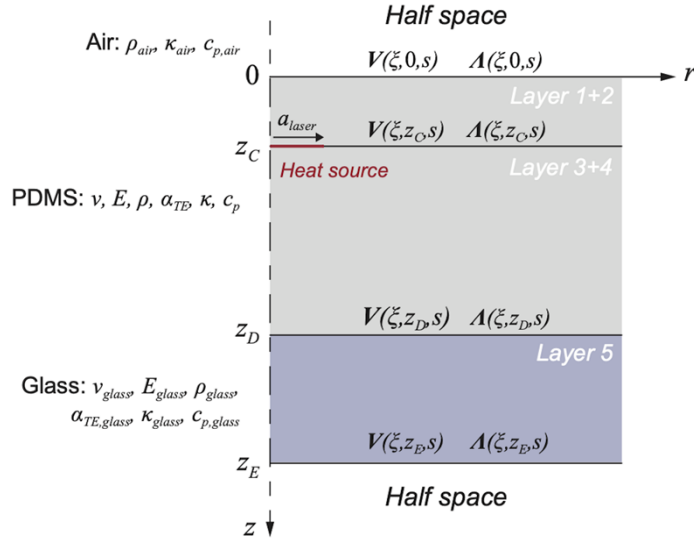


Fig. S2. Stress (\mathbf{V}) and displacement ($\mathbf{\Lambda}$) vectors in the Hankel-Laplace domain for the layered system. PDMS Layers 1 and 2, and 3 and 4 are combined. The surface heat source is located at depth z_C .

The continuity conditions at interfaces between layers, in the absence of external forces or heat sources, implies that:

$$\mathbf{V}(\xi, 0^-, s) = \mathbf{V}(\xi, 0^+, s), \quad (\text{S76})$$

$$\mathbf{V}(\xi, z_D^-, s) = \mathbf{V}(\xi, z_D^+, s), \quad (\text{S77})$$

$$\mathbf{V}(\xi, z_E^-, s) = \mathbf{V}(\xi, z_E^+, s), \quad (\text{S78})$$

$$\mathbf{\Lambda}(\xi, 0^-, s) = \mathbf{\Lambda}(\xi, 0^+, s), \quad (\text{S79})$$

$$\mathbf{\Lambda}(\xi, z_C^-, s) = \mathbf{\Lambda}(\xi, z_C^+, s), \quad (\text{S80})$$

$$\mathbf{\Lambda}(\xi, z_D^-, s) = \mathbf{\Lambda}(\xi, z_D^+, s), \quad (\text{S81})$$

$$\mathbf{\Lambda}(\xi, z_E^-, s) = \mathbf{\Lambda}(\xi, z_E^+, s). \quad (\text{S82})$$

At the depth z_C , the boundary condition is:

$$\mathbf{V}(\xi, z_C^+, s) = \mathbf{V}(\xi, z_C^-, s) + \mathbf{F}(\xi, z_C, s), \quad (\text{S83})$$

where the heat source is located. The external heat source is expressed as:

$$\mathbf{F}(\xi, z_C, s) = \begin{bmatrix} 0 & 0 & \tilde{Q}_e^0(\xi, z_C, s) \end{bmatrix}, \quad (\text{S84})$$

where $\tilde{Q}_e^0(\xi, z_C, s)$ is the HL transform of the external heat flow $Q_e(r, t)$ brought by laser irradiation. Following the surface heat source description (equation 4 in the main text):

$$q_e(r, t) = q_0 \phi_{laser}(r, t), \quad (\text{S85})$$

where:

$$\phi_{laser}(r, t) = (H(t) - H(t - t_0)) \times \left(H(a_{laser} - r) * \frac{1}{2\pi\sigma_{defocus}} e^{-\frac{r^2}{2\sigma_{defocus}^2}} \right), \quad (\text{S86})$$

we obtain:

$$\tilde{Q}_e^0(\xi, z_C, s) = \frac{1}{s} \tilde{q}_e^0(\xi, s) = \frac{q_0 a J_1(\xi a) (1 - e^{-t_0 s})}{\xi s^2} e^{-\frac{\sigma_{defocus}^2 \xi^2}{2}}. \quad (\text{S87})$$

We apply additional boundary conditions, which includes the absence of stress at the air/glass and air/PDMS boundaries. We, however, consider heat transfer at the top interface and ignore it at the bottom interface, which is far from the measurement planes so:

$$\mathbf{V}(\xi, 0, s) = [0, 0, \tilde{Q}^0(\xi, 0, s)]^T, \quad (\text{S88})$$

$$\mathbf{V}(\xi, z_E, s) = 0, \quad (\text{S89})$$

leading to:

$$\mathbf{K}^{(+\infty)} = 0, \quad (\text{S90})$$

$$\mathbf{K}^{(-\infty)} = \begin{bmatrix} 0 & 0 & 0 \\ 0 & 0 & 0 \\ 0 & 0 & -\kappa p / s \end{bmatrix}. \quad (\text{S91})$$

Although the surface heat transfer with air is relatively small, it will be important to model it in the eye as the retina is in contact with the vitreous, which has a higher thermal conductivity

than air. Rewriting $\mathbf{K}^{(1,2)}$ as $\mathbf{K}^{(1,2)} = \begin{bmatrix} \mathbf{A}^{(1,2)} & \mathbf{B}^{(1,2)} \\ \mathbf{C}^{(1,2)} & \mathbf{D}^{(1,2)} \end{bmatrix}$ and likewise for $\mathbf{K}^{(3,4)}$ and $\mathbf{K}^{(5)}$, we can

derive the state vectors of interest $\Lambda(\xi, 0, s)$ and $\Lambda(\xi, z_C, s)$ from equations S63–66 and S76–83:

$$\begin{bmatrix} \Lambda(\xi, 0, s) \\ \Lambda(\xi, z_C, s) \\ \Lambda(\xi, z_D, s) \\ \Lambda(\xi, z_C, s) \end{bmatrix} = \begin{bmatrix} \mathbf{K}^{(-\infty)} + \mathbf{A}^{(1,2)} & \mathbf{B}^{(1,2)} & \mathbf{0}_{3 \times 3} & \mathbf{0}_{3 \times 3} \\ \mathbf{C}^{(1,2)} & \mathbf{D}^{(1,2)} + \mathbf{A}^{(3,4)} & \mathbf{B}^{(3,4)} & \mathbf{0}_{3 \times 3} \\ \mathbf{0}_{3 \times 3} & \mathbf{C}^{(3,4)} & \mathbf{D}^{(3,4)} + \mathbf{A}^{(5)} & \mathbf{B}^{(5)} \\ \mathbf{0}_{3 \times 3} & \mathbf{0}_{3 \times 3} & \mathbf{C}^{(5)} & \mathbf{D}^{(5)} \end{bmatrix}^{-1} \begin{bmatrix} \mathbf{0}_{3 \times 1} \\ -\mathbf{F} \\ \mathbf{0}_{3 \times 1} \\ \mathbf{0}_{3 \times 1} \end{bmatrix} \quad (\text{S92})$$

For an intermediate plane located at a depth z_I between the planes A and C, the state vector is:

$$\Lambda(\xi, z_I, s) = -\left(\mathbf{D}^{(1,2)}(\xi, z_I, s) + \mathbf{A}^{(1,2)}(\xi, z_C - z_I, s) \right)^{-1} \left(\mathbf{C}^{(1,2)}(\xi, z_I, s) \Lambda(\xi, 0, s) + \mathbf{B}^{(1,2)}(\xi, z_C - z_I, s) \Lambda(\xi, z_C, s) \right). \quad (\text{S93})$$

230 We recall that to calculate $\overline{AA}(r, t)$ we need to calculate $u_z(r, z_A, t)$ at plane A for which
 231 $\Lambda(\xi, 0, s)$ is used. To calculate $\overline{AC}(r, t)$, we not only need $u_z(r, z_A, t)$ and $u_z(r, z_C, t)$, which
 232 require $\Lambda(\xi, 0, s)$ and $\Lambda(\xi, z_C, s)$, but also $\overline{\Delta n}$ or the average temperature rise θ between the
 233 planes A and C, which requires $\Lambda(\xi, z_I, s)$. We determined that the calculating this solution
 234 vector for 40 evenly-spaced depths between A and C was sufficient to ensure convergence of
 235 $\overline{\Delta n}$.

236 Having established the complete solutions for the displacements and the temperature rise in the
 237 HL domain, the spatial and time domains solutions can be found by numerical inversion of the
 238 Hankel and Laplace transforms, where both can be treated independently. For the Laplace
 239 transform, the Abate-Whitt framework [4] is a commonly used set of methods in which the
 240 inverse transform f is described by a linear combination of transformed values:

$$241 \quad f(t) \approx \sum_{k=1}^N \frac{\eta_k}{t} \bar{f}\left(\frac{\beta_k}{t}\right), \quad t > 0, \quad (S94)$$

242 where \bar{f} is the Laplace transform of f , the nodes β_k and weights η_k are N -dependent real
 243 or complex numbers. The precision of the inversion increases with N . Common methods in
 244 this framework include the Gaver-Stehfest, the Euler, and the Talbot method but all have been
 245 shown to be numerically unstable when inverting discontinuous functions, such as the square
 246 function [5,6]. We used instead a more recently developed method, which uses concentrated
 247 matrix exponential (CME) distribution and demonstrates remarkable stability and accuracy for
 248 discontinuous functions [6]. The β_k and η_k parameters are made available by the authors of
 249 [6].

250 The inverse Hankel transform of $\hat{f}(\xi)$ is defined by the integral:

$$251 \quad f(r) = \int_0^{+\infty} \hat{f}(\xi) J_m(\xi r) \xi d\xi, \quad (S95)$$

252 which can be split into intervals $[\xi_i, \xi_{i+1}]$:

$$253 \quad \int_0^{+\infty} \hat{f}(\xi) J_m(\xi r) \xi d\xi = \sum_{i=0}^{\infty} \int_{\xi_i}^{\xi_{i+1}} \hat{f}(\xi) J_m(\xi r) \xi d\xi \approx \sum_{i=0}^{N_B} \int_{\xi_i}^{\xi_{i+1}} \hat{f}(\xi) J_m(\xi r) \xi d\xi, \quad (S96)$$

254 where ξ_i represent the zero points of the Bessel function J_m . The integrals over the intervals
 255 $[\xi_i, \xi_{i+1}]$ can then be approximated using the Gauss-Legendre quadrature with:

$$256 \quad \int_{\xi_i}^{\xi_{i+1}} \hat{f}(\xi) J_m(\xi r) \xi d\xi = \frac{\xi_{i+1} - \xi_i}{2} \sum_{p=1}^{N_{GL}} w_p \hat{f}(\beta_k) J_m(r \beta_k) \beta_k, \quad (S97)$$

$$257 \quad \beta_k = \left(\frac{\xi_{i+1} - \xi_i}{2} \right) r_p + \left(\frac{\xi_{i+1} + \xi_i}{2} \right), \quad (S98)$$

258 where w_p and r_p are the Gaussian weights and nodes, respectively [7]. The accuracy of the
 259 numerical integration increases with the number of Bessel intervals considered (N_B) and the
 260 quadrature order N_{GL} (see the following section for numerical inversion convergence study).
 261

262 3. Stiffness matrix method (SMM) validation using FEM simulations

263 To validate the SMM calculations, we used an axisymmetric finite-element model of the tissue
 264 phantom implemented in the finite element method (FEM) software COMSOL. The model
 265 included all the phantom layers listed in Table 1 and a finite air layer at the top of the assembly,
 266 in contact with plane A. Contrary to SMM, the model must be of finite size in all dimensions,
 267 so the air layer was chosen to have a thickness 500- μm and the width of the domain was 2000
 268 μm ($10 \times$ the heating beam radius). The bottom interface (glass) was considered to be thermally
 269 isolated. The temperature was set at room temperature on the other boundaries.

270 The boundary heat source was modeled following the Beer-Lambert law as described in the
 271 Materials and Methods, equation 4:

$$272 \quad q_e(r, t) = \frac{P_0}{\pi a^2} \phi_{laser}(r, t) (1 - e^{-\mu_a l}). \quad (\text{S99})$$

273 We here omitted for validation purposes the Gaussian blur in the spatial profile of the beam
 274 and considered a square pulse in time with a top-hat profile in space.

$$275 \quad \phi_{laser}(r, t) = (H(t) - H(t - t_0)) \times H(a_{laser} - r). \quad (\text{S100})$$

276 The validation was performed using the fitted material parameters listed in Table 2. The
 277 COMSOL model included the solid mechanics module with linear elasticity equations, the heat
 278 transfer module, and the thermal expansion multi-physics module. The mesh was defined using
 279 the extremely-fine physics-controlled mesh provided by COMSOL to ensure element size
 280 convergence. The model is available as Dataset 2. In Fig. S3a, we compare the vertical
 281 displacements at the center ($r = 0$) of plane A ($z = z_A$) obtained from COMSOL simulations and
 282 calculated by SMM using high-order inverse integrations for both the Hankel and Laplace
 283 inverse transforms (20 Bessel intervals ($B=20$), 20-point Gauss-Legendre quadrature ($G=20$),
 284 20th order inverse Laplace with concentrated matrix exponential distributions ($C=20$)). We thus
 285 verify the good match between the calculation methods. We note short-lived oscillations (μs
 286 timescale) in COMSOL results corresponding to the establishment of the mechanical
 287 equilibrium (wave reflections) that are absent in SMM results. The time-dependent term in the
 288 wave equation is ignored in the governing equations for SMM (equations S13 and S14) as the
 289 wave dynamics are too fast to be captured using the OCT system. We also note a faster recovery
 290 of u_z in COMSOL, which is attributed to boundary effects in COMSOL (finite air thickness
 291 and finite width).

292 Having verified the accuracy of the SMM calculations at high integration orders, we studied
 293 the effect of integration orders of the precision on the results. Since the computation time
 294 depends on these orders, we aimed to select low orders giving reasonable accuracy and
 295 precision. The error between the high-order calculations ($B=20$, $G=20$, $C=20$) and lower-order
 296 calculations is shown in Fig. S3b. We estimated that convergence below 1% error occurs for
 297 $B \geq 5$, $G \geq 6$, and $C \geq 7$. These orders ($B=5$, $G=6$, $C=7$) were therefore selected for the fitting
 298 procedure.

299 For a simulated duration of 200 ms, with 0.1-ms time intervals, the computation time for
 300 COMSOL was about 30 minutes. Using SMM and selected orders, for the same time points
 301 (2001 points), and for one radial point ($r = 0$), the computation took 70 seconds on a laptop
 302 computer, which demonstrates the increased computation efficiency using SMM.

303

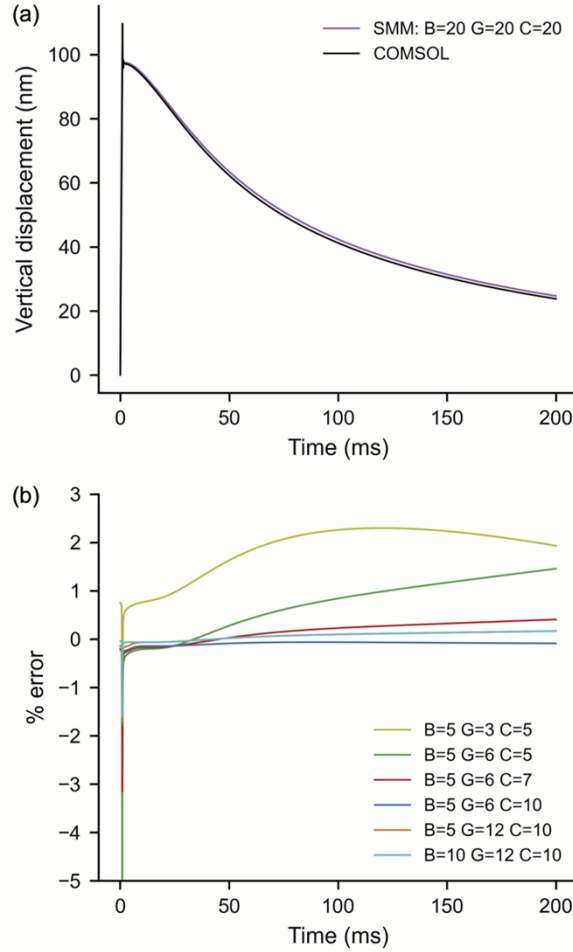


Fig S3. (a) Vertical displacements u_z calculated at ($r = 0, z_A = 0$) with COMSOL and stiffness matrix method (SMM) with 20 Bessel intervals ($B=20$) and a 20-point Gauss-Legendre quadrature of 20 ($G=20$) for the inverse Hankel transform and a concentrated matrix exponential order of 20 ($C=20$) for the inverse Laplace transform. (b) Error between high-order inverse HL transform ($B=20, G=20, C=20$) and lower-order inverse transforms.

4. Elastic modulus effects on thermal expansion

We evaluated the influence of the elastic modulus on the thermo-mechanical response by running SMM calculations varying the elastic modulus by a factor of 2 from the initial of $E = 1.3$ MPa found in the literature [8]. Results are shown in Fig. S4. As one can expect, the elastic modulus has no effect on the temperature rise at the absorption layer (Fig. S4a). Additionally, the effect is also negligible on the vertical displacements u_z , as illustrated in Fig. S4b, which shows the vertical displacement calculated at ($r = 0, z = 0$). We could therefore set the elastic modulus at 1.3 MPa and not fit it.

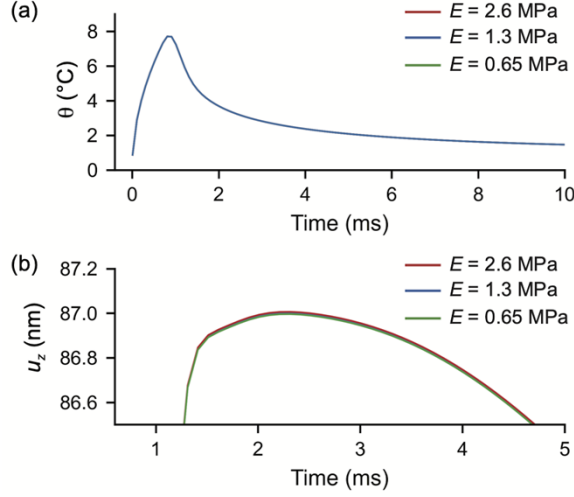


Fig. S4. Effects of the PDMS elastic modulus on the tissue model response. (a) E has no effect on the temperature rise (θ). All curves overlap and are undistinguishable. (b) E has little effect on the vertical displacement response.

5. Material property fitting procedure

The raw OCT data after calculations of the Δ OPLs, which removes the z dimension, has 521 points in radius and 5001 points in time. This corresponds to a radial extent of ± 1150 μm and a duration of 500 ms. As we fitted the $\overline{\text{AA}}$ data first, we cropped the dataset radially to a smaller window of ± 500 μm , which encompassed the highest SNR data points, which are most useful for fitting. We then performed a spatial average between positive and negative radii and a temporal rolling average using a rolling window of 5 time points. Because the rolling average correlate noise in the rolling window, we extracted a subset of time points to preserve uncorrelated-noise data. We also cropped the data in time starting shortly after the end of the heating pulse (1.5 ms), after which the data varied slowly so that the rolling average did not erase high-frequency features. At this delay, the surface and the volumetric heat sources can be considered equivalent. The $\overline{\text{AA}}$ dataset at this stage was composed of 111 points in space and 961 points in time. As explained in the main text, by fitting $\overline{\text{AA}}$ we can determine the parameters κ , σ_{defocus} , a_{laser} and the proportionality factor γ to the product $\alpha_{\text{TE}} \times q_0$ with $(\alpha_{\text{TE}} q_0)_{\text{fitted}} = \gamma (\alpha_{\text{TE}} q_0)_{\text{initial}}$.

Because the fitting computation time depends on the number of experimental data points considered, we then aimed to determine the minimum number of points that would ensure accurate fitting. To do so, we down-selected an array of n -by- n points (starting at 4×4 points), performed non-linear least square fitting on this dataset, got the fitted parameters, used the fitted parameters to calculate the modeled $\overline{\text{AA}}$ on the full dataset domain (111×961 points), and computed the root-mean-square error (RMSE) between the modeled and the full experimental $\overline{\text{AA}}$ dataset. Then a new n -by- n points dataset was extracted from the full dataset with a higher n and fitting operations were repeated. It is expected that the RMSE will tend to decrease as we included more experimental data points (as n increased) in the fitting. When the RMSE plateaued with increasing n , we could consider that additional data points would not bring added accuracy or precision. We therefore stopped at this n value. We found that 22×22 $\overline{\text{AA}}$ points were sufficient to obtain acceptable fitting.

352 To estimate the uncertainties on the parameters κ , $\sigma_{defocus}$, a_{laser} , and γ , the experimental data
 353 were bootstrapped to simulate 200 experimental datasets. The fitting was then repeated 200
 354 times and we obtained 200-element arrays of fitted κ , $\sigma_{defocus}$, a_{laser} , and γ values. The best fit
 355 values were calculated by averaging the 200 fitted values and the uncertainties were obtained
 356 from the standard deviations. The fitted values also served to evaluate the correlation between
 357 the parameters (see the following Parameter correlation section).

358 Using κ , $\sigma_{defocus}$, a_{laser} , and γ found by fitting \overline{AA} we calculated the modeled \overline{AC} by applying
 359 the γ factor to q_0 . Here we aimed to find the independent and respective γ_i values for q_0 and α_{TE}
 360 with:

$$361 \quad (\alpha_{TE})_{fitted} = \gamma_1 (\alpha_{TE})_{initial} , \quad (S101)$$

$$362 \quad (q_0)_{fitted} = \gamma_2 (q_0)_{initial} , \quad (S102)$$

$$363 \quad \gamma = \gamma_1 \times \gamma_2 . \quad (S103)$$

364 Because \overline{AC} scales linearly with q_0 but not α_{TE} , fitting a scaling factor between the modeled
 365 and the experimental \overline{AC} meant find the η factor with:

$$366 \quad (q_0)_{fitted} = \eta \gamma (q_0)_{initial} , \quad (S104)$$

367 which therefore allowed the determination of γ_1 and γ_2 :

$$368 \quad \gamma_2 = \eta \gamma , \quad (S105)$$

$$369 \quad \gamma_1 = 1 / \eta . \quad (S106)$$

370 \overline{AC} was also reduced to the same 22×22 points and bootstrapped 200 times to find the
 371 constant η and its corresponding uncertainty. At this point the five fitting parameters κ , $\sigma_{defocus}$,
 372 a_{laser} , q_0 (therefore μ_a) and α_{TE} were fully determined along with their uncertainties. The values
 373 are reported in Table 3. The full procedure is shown schematically in Fig. S5. The residuals
 374 obtained after fitting of \overline{AA} and \overline{AC} are shown in Fig. S6.

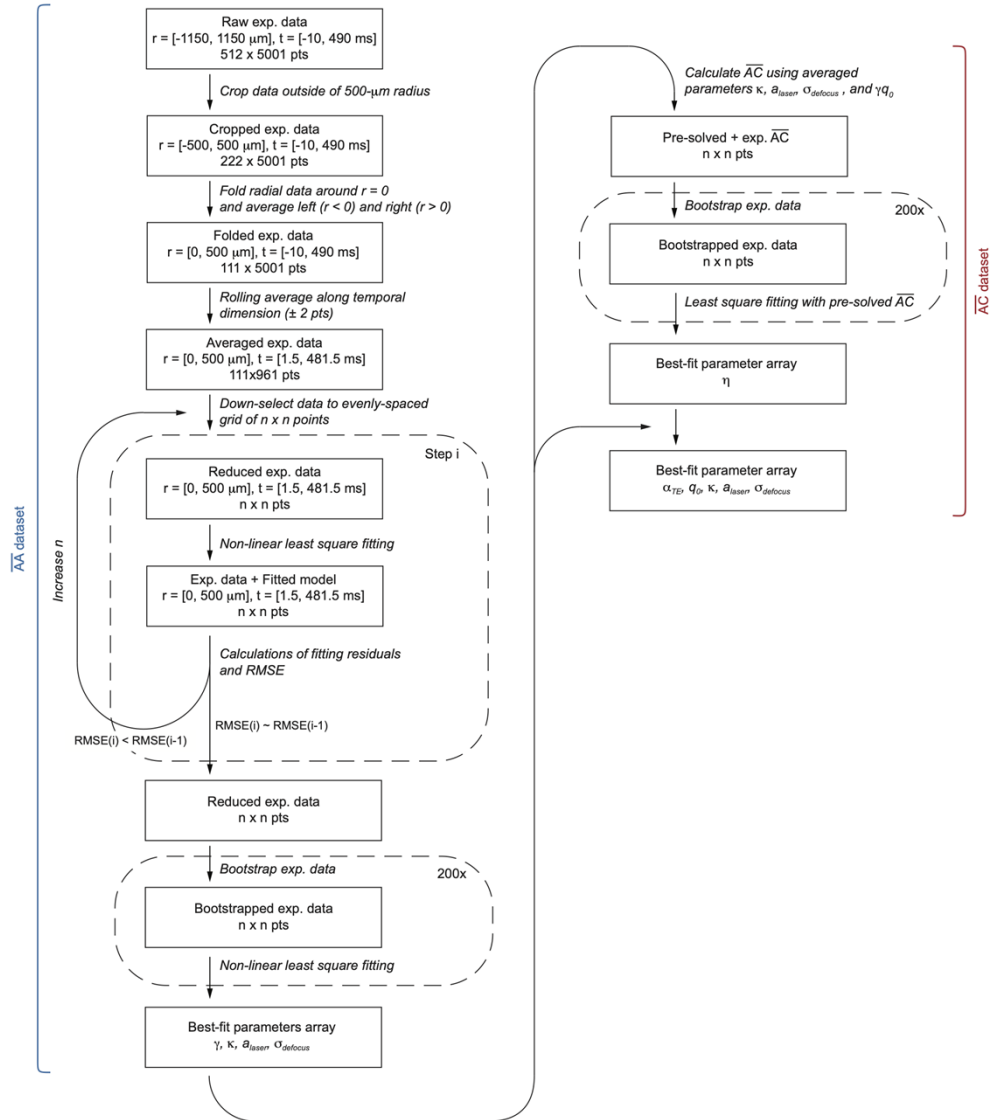


Fig. S5. Data reduction and fitting procedure.

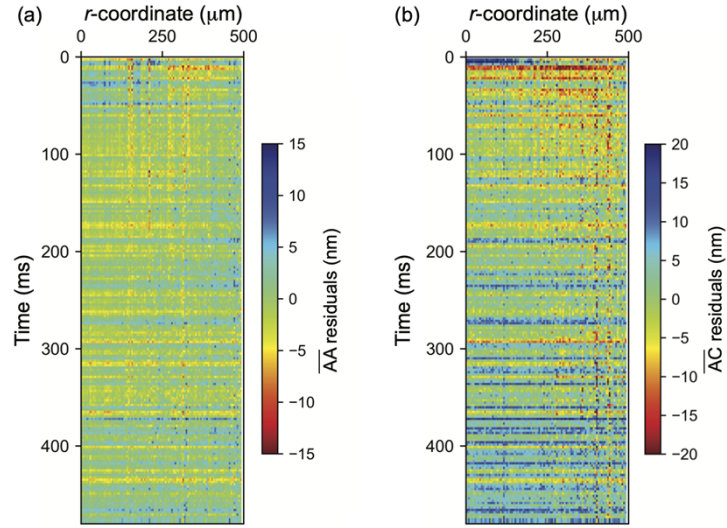


Fig. S6. Residuals between modeled and experimental Δ OPLs.

6. Parameter correlations

Through fitting of bootstrapped experimental data (200 times), it is possible to evaluate the cross-correlation between the fitting parameters. The correlation between parameters can be visualized by plotting the result of the 200 fits for all pairs of parameters (6 pairs for 4 variables) (Fig. S7). Low correlation is indicated by the absence of high-eccentricity ellipses not aligned with the parameter axes.

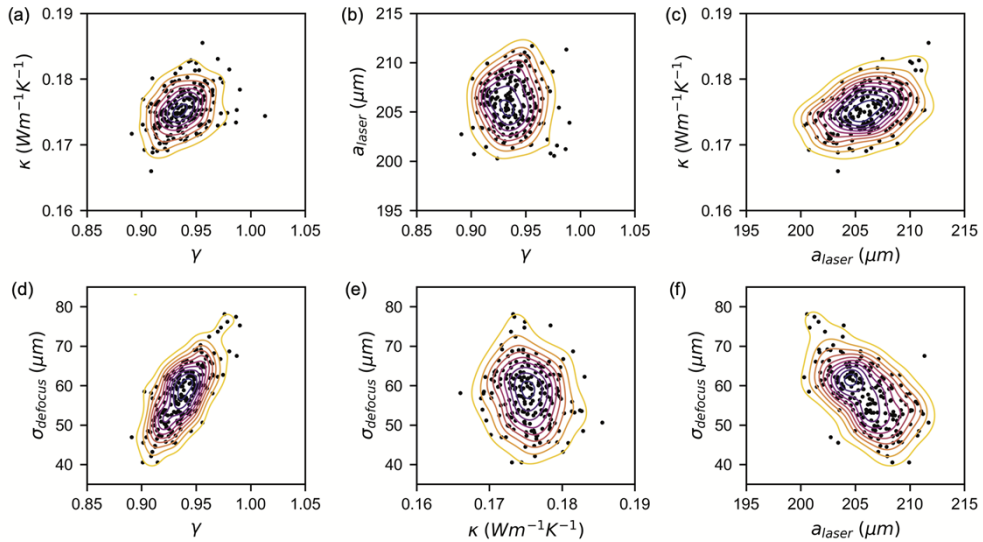


Fig. S7. Correlations between fitted parameter values obtained by bootstrapping. Local densities, indicated by the contour maps, were estimated using a Gaussian kernel.

390 7. Non-damaging treatment range

391 As described in the Materials and Methods section, the Arrhenius integral can be used to define
392 the therapeutic window and determine the laser power titration. It can be expressed as [9]:

$$393 \quad \Omega(r, t) = A \int_0^t e^{-\frac{E^*}{R \times T(t)}} dt, \quad (S107)$$

394 where A ($1.6 \times 10^{55} \text{ s}^{-1}$) is the rate constant, E^* (340 kJ/mol) is the activation energy, R (8.314
395 J.K⁻¹.mol⁻¹) is the gas constant and T is the temperature as a function of time. We here looked
396 at the influence of the absorption coefficient on the integral value in order to estimate the
397 precision required on this material parameter to allow non-damaging therapy. We ran
398 COMSOL simulations similar to what is done to validate the stiffness matrix method with the
399 tissue phantom (see Stiffness matrix method (SMM) validation using FEM simulations section
400 in the SI). The retina was modeled as rat retina composed of multi-layered isotropic media
401 whose top surface is in contact with a liquid (modeled as water) representing the vitreous fluid.
402 The layer thicknesses and material properties used in the simulations are listed in Table S1 with
403 the corresponding references. The COMSOL model is available as Dataset 1. In COMSOL, the
404 retinal layers were modeled as linear elastic layers and the vitreous a Newtonian fluid. Heat
405 transfer was allowed at the liquid/solid interface. The external heat source was modeled
406 following the Beer-Lambert law with the heat flux given by:

$$407 \quad q_e(r, z, t) = \frac{P_0}{\pi a_{laser}^2} \phi_{laser}(r, t) \mu_a(z) e^{-\mu_a(z)z}, \quad (S108)$$

408 where P_0 is the incident laser power at the top of the absorbing layer, a_{laser} is the radius of the
409 top-hat intensity profile, ϕ_{laser} is the spatio-temporal profile of the laser beam described below
410 and μ_a is the optical absorption coefficient. For the non-pigmented choroid (NPC) and the
411 pigmented choroid (PC) layers, P_0 was calculated taking into account the absorption of the
412 preceding layers. The beam spatio-temporal profile ϕ_{laser} was modeled as a square pulse in time
413 with duration $t_0 = 10 \text{ ms}$ and top-hat profile in space with radius $a_{laser} = 200 \mu\text{m}$, which are
414 typical parameters used in retinal therapy [10]:

$$415 \quad \phi_{laser}(r, t) = (H(t) - H(t - t_0)) \times H(a_{laser} - r), \quad (S109)$$

416 where H is the Heaviside function. The initial absorption coefficient values $\mu_{a,0}$ are taken from
417 literature [11]. Using initial values, P_0 was adjusted to 55 mW so that $\Omega \approx 0.5$ (about the center
418 of the therapeutic window), which was calculated using the temperature course $T(t)$ at the
419 hottest point in space (top of the retinal pigment epithelium (RPE) layer in depth, center of the
420 beam in radius) (Fig S8a). The absorption coefficients μ_a was then varied and the Arrhenius
421 integral was calculated (Fig S8b). Such study allows us to determine the acceptable precision
422 on μ_a to remain in the therapeutic window. We found that a variation of about 20% from the
423 initial values reached the limits of the window, which corresponded to a peak temperature
424 difference of $\pm 4^\circ\text{C}$.

425

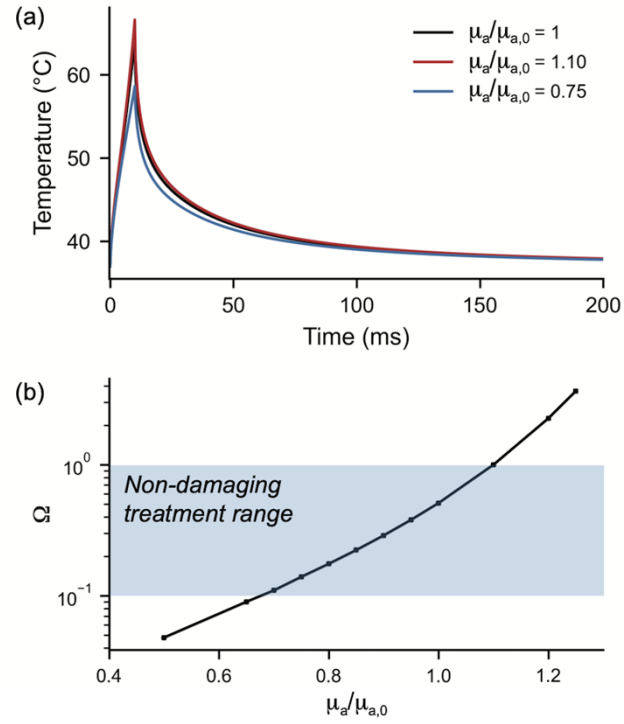


Fig. S8. (a) Temperature profiles at the top of the RPE layer and center of the beam for three absorption coefficient values. (b) Arrhenius integral calculated as a function of the absorption coefficient value μ_a relative to its initial value $\mu_{a,0}$. The non-damaging treatment range is $0.1 < \Omega < 1$.

431 Table S1. Retina model parameters used in COMSOL simulations for temperature calculations. NFL: nerve
 432 fiber layer, GCL: ganglion cell layer, IPL: inner plexiform layer, INL: inner nuclear layer, OPL: outer
 433 plexiform layer, ONL: outer nuclear layer, PR: photoreceptor layer, RPE: retinal, PC: pigmented choroid,
 434 NPC: non-pigmented choroid. h : layer thickness, ρ : density, E : Young's modulus, α_{TE} : coefficient of thermal
 435 expansion, ν : Poisson's ratio, κ : coefficient of thermal conductivity, c_p : specific heat capacity, μ_a : coefficient of
 436 optical absorption.
 437

	h (μm)	ρ ($\text{kg}\cdot\text{m}^{-3}$)	E (kPa)	α_{TE} (K^{-1})	ν	κ ($\text{W}\cdot\text{m}^{-1}\cdot\text{K}^{-1}$)	c_p ($\text{J}\cdot\text{kg}^{-1}\cdot\text{K}^{-1}$)	μ_a (cm^{-1}) ^b
Water (vitreous)	300	993 ^a	NA	3.45×10^{-4} ^a	NA	0.63 ^a	4180 ^a	-
NFL-GCL	30 [12]		1.3 [13]		0.47 [14]	0.45 [15]	3600 [16]	-
IPL	30 [12]		1.3 [13]					-
INL	20 [12]		2.7 [13]					-
OPL	10 [12]		8 [13]					-
ONL	65 [12]		2.7 [13]					-
PR	40 [12]		26 [13]					-
RPE melanosomes	1 [11]		5 [17]				9.976×10^3 [11]	-
RPE basal	3 [11]		5 [17]					-
PC	20 [11]		30 [17]					2.494×10^3 [11]
NPC	30 [11]		30 [17]					475 [11]
Sclera	500 [11]		30 [17]				3200 [16]	-

438 ^awww.engineeringtoolbox.com. Data taken at 37°C. ^bSmall absorption coefficients ($<1 \text{ cm}^{-1}$) are ignored. The
 439 references are indicated next to the values.
 440

441 Dataset legends

442 Dataset 1. Java source code for thermo-mechanical modeling of a rat retina. The model was used to study the influence
 443 of the optical absorption coefficient on the Arrhenius integral as described in the section "Non-damaging treatment

range" of the Supplemental Document. The code can be compiled for COMSOL following instructions at <https://www.comsol.com/blogs/automate-modeling-tasks-comsol-api-use-java/>.

Dataset 2. Java source code for thermo-mechanical modeling of the tissue phantom. The model was used to validate the stiffness matrix methods as described in the section "Stiffness matrix method (SMM) validation using FEM simulations" of the Supplemental Document. The code can be compiled for COMSOL following instructions at <https://www.comsol.com/blogs/automate-modeling-tasks-comsol-api-use-java/>.

References

1. M. A. A. Biot, "Thermoelasticity and Irreversible Thermodynamics," *J. Appl. Phys.* **27**(3), 240–253 (1956).
2. B. Davies, *Integral Transforms and Their Applications*, Second Edi, Applied Mathematical Sciences (Springer New York, 1985), **25**.
3. Z. Y. Ai, Z. Zhao, and L. J. Wang, "Thermo-mechanical coupling response of a layered isotropic medium around a cylindrical heat source," *Comput. Geotech.* **83**, 159–167 (2017).
4. J. Abate and W. Whitt, "A Unified Framework for Numerically Inverting Laplace Transforms," *INFORMS J. Comput.* **18**(4), 408–421 (2006).
5. M. Raoofian Naeeni, R. Campagna, M. Eskandari-Ghadi, and A. A. Ardalan, "Performance comparison of numerical inversion methods for Laplace and Hankel integral transforms in engineering problems," *Appl. Math. Comput.* **250**, 759–775 (2015).
6. G. Horváth, I. Horváth, S. A. D. Almousa, and M. Telek, "Numerical inverse Laplace transformation using concentrated matrix exponential distributions," *Perform. Eval.* **137**, 102067 (2020).
7. P. Cornille, "Computation of Hankel Transforms," *SIAM Rev.* **14**(2), 278–285 (1972).
8. I. D. Johnston, D. K. McCluskey, C. K. L. Tan, and M. C. Tracey, "Mechanical characterization of bulk Sylgard 184 for microfluidics and microengineering," *J. Micromechanics Microengineering* **24**(3), 035017 (2014).
9. C. Sramek, Y. Paulus, H. Nomoto, P. Huie, J. Brown, and D. Palanker, "Dynamics of retinal photocoagulation and rupture," *J. Biomed. Opt.* **14**(3), 034007 (2009).
10. D. Lavinsky, C. Sramek, J. Wang, P. Huie, R. Dalal, Y. Mandel, and D. Palanker, "Subvisible retinal laser therapy: Titration algorithm and tissue response," *Retina* **34**(1), 87–97 (2014).
11. G. Goetz, T. Ling, T. Gupta, S. Kang, J. Wang, P. D. Gregory, B. Hyle Park, and D. Palanker, "Interferometric mapping of material properties using thermal perturbation," *Proc. Natl. Acad. Sci. U. S. A.* **115**(11), E2499–E2508 (2018).
12. V. J. Srinivasan, T. H. Ko, M. Wojtkowski, M. Carvalho, A. Clermont, S. E. Bursell, H. S. Qin, J. Lem, J. S. Duker, J. S. Schuman, and J. G. Fujimoto, "Noninvasive volumetric imaging and morphometry of the rodent retina with high-speed, ultrahigh-resolution optical coherence tomography," *Investig. Ophthalmol. Vis. Sci.* **47**(12), 5522–5528 (2006).
13. Y. Qu, Y. He, Y. Zhang, T. Ma, J. Zhu, Y. Miao, C. Dai, M. Humayun, Q. Zhou, and Z. Chen, "Quantified elasticity mapping of retinal layers using synchronized acoustic radiation force optical coherence elastography," *Biomed. Opt. Express* **9**(9), 4054 (2018).
14. Y. B. Lu, K. Franze, G. Seifert, C. Steinhäuser, F. Kirchhoff, H. Wolburg, J. Guck, P. Janmey, E. Q. Wei, J. Käs, and A. Reichenbach, "Viscoelastic properties of individual glial cells and neurons in the CNS," *Proc. Natl. Acad. Sci. U. S. A.* **103**(47), 17759–17764 (2006).
15. F. Härting and U. Pfeiffenberger, "Thermal conductivity of bovine and pig retina: An experimental study," *Graefe's Arch. Clin. Exp. Ophthalmol.* **219**(6), 290–291 (1982).
16. E. B. Felstead and R. S. C. Cobbold, "Analog solution of laser retinal coagulation," *Med. Electron. Biol. Eng.* **3**(2), 145–155 (1965).
17. Y. Qu, Y. He, A. Saidi, Y. Xin, Y. Zhou, J. Zhu, T. Ma, R. H. Silverman, D. S. Minckler, Q. Zhou, and Z. Chen, "In vivo elasticity mapping of posterior ocular layers using acoustic radiation force optical coherence elastography," *Investig. Ophthalmol. Vis. Sci.* **59**(1), 455–461 (2018).